Supplement of

Seasonal Secondary and Biomass-Burning Aerosol Sources and Enhancements of Cloud Condensation Nuclei at a Central US Background Site

Maria A. Zawadowicz[1], Amie Dobracki[2], Janek Uin[1], Rebecca Trojanowski[3]

[1]Environmental Science and Technologies, Brookhaven National Laboratory, Upton, NY 11973
[2]Rainmaker Technology Corporation, El Segundo, CA 90245
[3]Interdisciplinary Science, Brookhaven National Laboratory, Upton, NY 11973

Correspondence to: Maria A. Zawadowicz (mzawadowi@bnl.gov)

S1 ACSM Data Processing and DQA

During the study period, the ACSM was calibrated six times. Response factors (RFs) were linearly interpolated between successive calibrations and applied to the intervening measurements. A composition-dependent collection efficiency (CDCE) correction following Middlebrook et al. (2012) was applied to all ACSM data. For closure analyses, ACSM component mass concentrations were converted to particle volume using the species densities listed in Table S1, dry scattering was estimated using species-specific mass scattering efficiencies (MSE), and aerosol hygroscopicity was calculated from component κ values.

Supplementary Table S1. Constants used in closure calculations.

	density (g cm^{-3})	κ	MSE
Sulfate	1.77	0.61	2.5
Nitrate	1.72	0.67	2.7
Ammonium	1.77	-	-
Chloride	1.35	-	3.7
BBOA	1	0.1	6
SVOOA	1.5	0.1	3.9
LVOOA	1.7	0.1	3.9

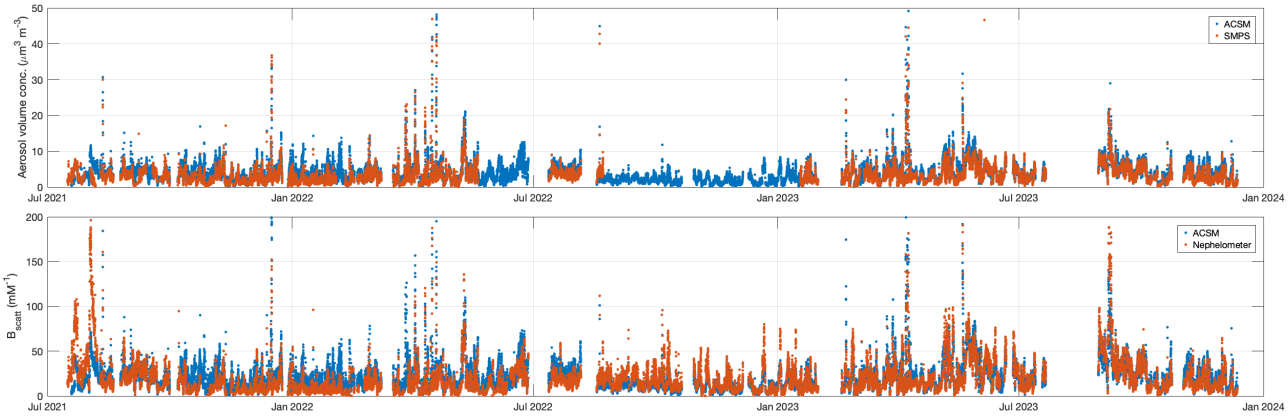

Supplemental Figure S1. Top: time series comparison of aerosol volume concentration derived from the ACSM and measured by the SMPS. Bottom: time series comparison of dry light-scattering coefficient estimated from ACSM composition and measured by the nephelometer.

The ACSM-derived NR-PM_1 mass and composition at SGP were evaluated against independent, co-located measurements to establish data quality. Figures S1-S2 show that ACSM-derived submicron aerosol burden agreed well with physical aerosol measurements. ACSM-derived NR-PM_1 volume closely tracked SMPS-derived submicron volume over the full record, with $R^2 = 0.73$ and a regression slope of 0.9, indicating that the ACSM captured most of the aerosol mass in the submicron size range. ACSM-derived dry scattering estimates were likewise consistent with nephelometer measurements ($R^2 = 0.6$, slope =

0.62), particularly during periods of elevated sulfate and organic aerosol loading. Some departures were observed during high-relative-humidity episodes, when aerosol liquid water contributed to nephelometer scattering but was not represented in ACSM dry mass. Overall, the agreement indicates robust mass closure and supports the quantitative accuracy of the ACSM measurements within expected uncertainty.

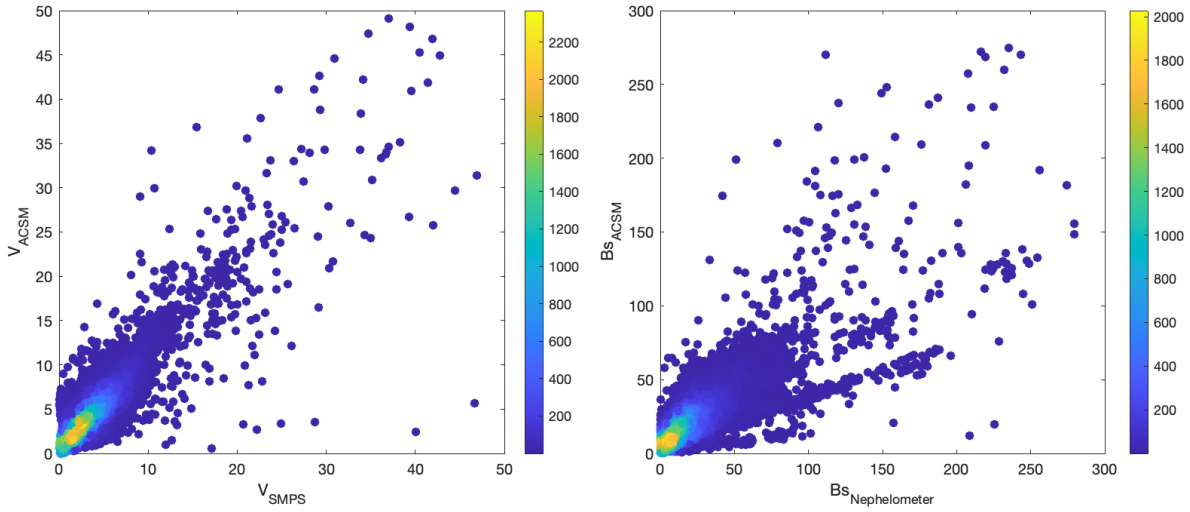

Supplemental Figure S2. Left: Density scatter plot comparing ACSM-derived NR-PM$_1$ volume concentration with SMPS submicron aerosol volume concentration. Right: Density scatter plot comparing dry light-scattering coefficient estimated from ACSM composition with the scattering coefficient measured by the nephelometer.

We assessed CCN closure by comparing measured CCN number concentrations with CCN concentrations predicted from the SMPS size distributions and ACSM composition using κ-Köhler theory and the component κ values listed in Table S1. Following Petters and Kreidenweis (2007), the internally mixed calculation uses a single bulk hygroscopicity parameter derived as the volume-weighted sum of the component κ values. The externally mixed calculation follows the framework used by Kulkarni et al. (2023), in which the aerosol population is treated as separate sulfate-, nitrate-, and organic-containing particles rather than as a uniformly mixed population. These two calculations therefore represent limiting assumptions on aerosol mixing state.

Figure S3 shows the probability density functions of the closure ratio expressed as $N_{CCN,measured}/N_{CCN,calculated}$ for SS = 0.1, 0.2, 0.4, 0.8, and 1.0%. A value of 1 indicates perfect closure, values below 1 indicate overprediction of CCN by the calculation, and values above 1 indicate underprediction. Across all supersaturations, both distributions are centered below unity, indicating that the predicted CCN concentrations are generally higher than those observed. The internally mixed calculation is systematically shifted farther below 1 than the externally mixed calculation, especially at 0.1-0.4% SS, showing that the internal-mixing assumption produces the larger overprediction. At 0.8% and 1.0% SS, the internally and externally mixed distributions converge, indicating that sensitivity to the κ treatment decreases as supersaturation increases. This interpretation

is consistent with prior work showing that CCN activation is sensitive to aerosol mixing state and that internal and external mixtures exhibit different activation behavior (Vu et al., 2019).

Taken together, Fig. S3 indicates that assuming a fully internal mixture makes the aerosol population too hygroscopic and leads to systematic overprediction of CCN, whereas allowing an external mixture improves closure, most clearly at low and intermediate supersaturation. The figure therefore does not support near-perfect closure across all SS. Instead, it shows that the CCN and composition measurements are broadly self-consistent, but that closure depends materially on the assumed aerosol mixing state. This behavior is consistent with Kulkarni et al (2023), who reported that external-mixture assumptions can provide better CCN closure than a fully internal-mixture treatment, while internal mixing achieved only modest closure under more limited conditions.

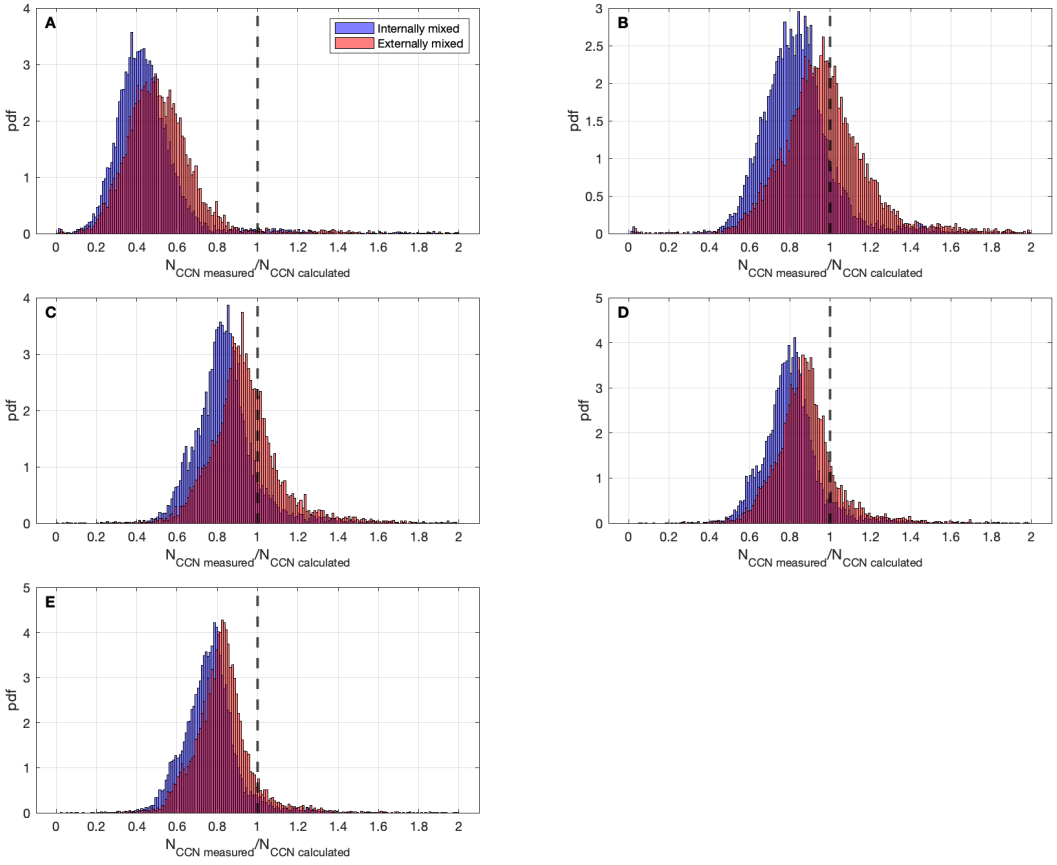

Supplemental Figure S3: Probability density functions of the measured-to-calculated CCN ratio, $\mathbf{N_{CCN,measured}/N_{CCN,calculated}}$, for CCN predictions using internally mixed (blue) and externally mixed (red) aerosol κ calculations. Panels correspond to supersaturations of (A) 0.1%, (B) 0.2%, (C) 0.4%, (D) 0.8%, and (E) 1.0%. The dashed vertical line marks unity; values less than 1 indicate CCN overprediction by the calculation. The internally mixed κ follows the standard volume-weighted treatment for multicomponent particles, whereas the externally mixed κ follows the separate-population treatment described by Kulkarni et al. (2023).

S2 PMF Procedure

To identify the major source profiles in the dataset and their associated temporal behavior, we performed Positive Matrix Factorization (PMF, Paatero and Tapper, 1994), a long-standing standard source apportionment technique in analysis of atmospheric aerosol mass spectrometry data (Ulbrich et al., 2009; Zhang et al., 2011). Briefly, in the bilinear mode used here, PMF describes the measured data matrix X as a product of two matrices, **G** and **F**, and the residual matrix **E**:

$$\mathbf{X} = \mathbf{GF} + \mathbf{E} \quad \text{(S1)}$$

Each column in matrix **G** represents the time series of a factor profile (mass spectrum) and each row in the matrix **F** represents the corresponding factor profile. In order to solve equation (S1), quantity Q is minimized with respect to all model variables:

$$Q = \sum_{i=1}^{n} \sum_{j=1}^{m} \left(\frac{e_{ij}}{\sigma_{ij}}\right)^2,$$

where **σ** corresponds to a matrix of measurement uncertainties of **X**.

In this study, we base the PMF approach on that described in Canonaco et al. (2021), in that we use the multilinear engine (ME-2, Paatero, 1999) algorithm, constrain certain profiles with reference mass spectra, and perform multiple PMF runs on a subset of data defined by a temporal window moved in 1d increments across the entire dataset ("rolling PMF" strategy). This method allows better capturing of seasonal variations in factor profiles (Canonaco et al., 2021). We carry out the PMF calculations using the Source Finder (SoFi) software package (Canonaco et al., 2013); however, the clustering and post-processing averaging steps were performed with custom routines written in MATLAB environment (MATLAB 2020b).

S2.1 Unconstrained Seasonal PMF

Before performing rolling PMF constrained with reference profiles, we carried out a series of unconstrained seasonal PMF runs in order to find out the likely set of reference profiles. The SGP quadrupole ACSM organic matrix and its associated error matrix generated by the Aerodyne ACSM Local software package were first averaged to 90 minutes sampling frequency, and then they were divided into four seasons: winter (December-February), spring (March-May), summer (June-August) and autumn (September-November). For each season, an unconstrained PMF run with random seeds was performed for three, four and five factors, 300 times each. Subsequently, each set of 300 PMF runs was then clustered using the k-means algorithm.

The optimized number of PMF profiles for each season is selected based on the calculated average silhouette value of the k-means clustering solution for 3, 4 and 5 factors. The silhouette value for each point is a measure of how similar that point is to other points in the same cluster, compared to points in other clusters. The silhouette value s_i for the i^{th} point is defined as

$$s_i = \frac{(b_i - a_i)}{\max(a_i, b_i)},$$

where a_i is the average distance from the i^{th} point to the other points in the same cluster as i, and b_i is the minimum average distance from the i^{th} point to points in a different cluster, minimized over the clusters. If the i^{th} point is the only point in its cluster, then the silhouette value s_i is set to 1. A high silhouette value indicates that the point is well matched to its own cluster, and poorly matched to other clusters. If most points have a high silhouette value, then the clustering solution is appropriate. If

many points have a low or negative silhouette value, then the clustering solution might have too many or too few clusters. We select the appropriate seasonal PMF solution based on the highest silhouette value (Supplemental Figures 1-4).

Supplemental Figures S4-S7 show average silhouette values for each seasonal PMF solution, a set of average reference profiles for the chosen seasonal solution and plots of key m/z markers for individual PMF runs in the chosen seasonal solution (f43, f44, f55, f57, and f60).

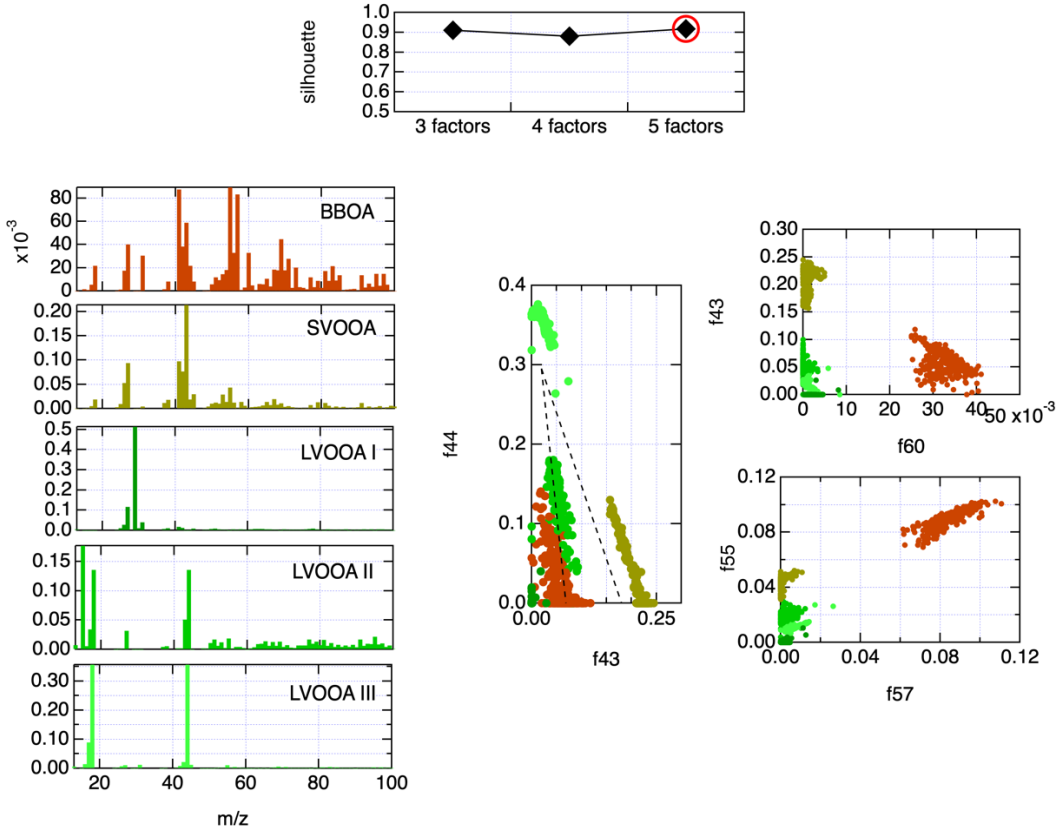

Supplemental Figure S4. K-means clustering results for December-February (winter) period.

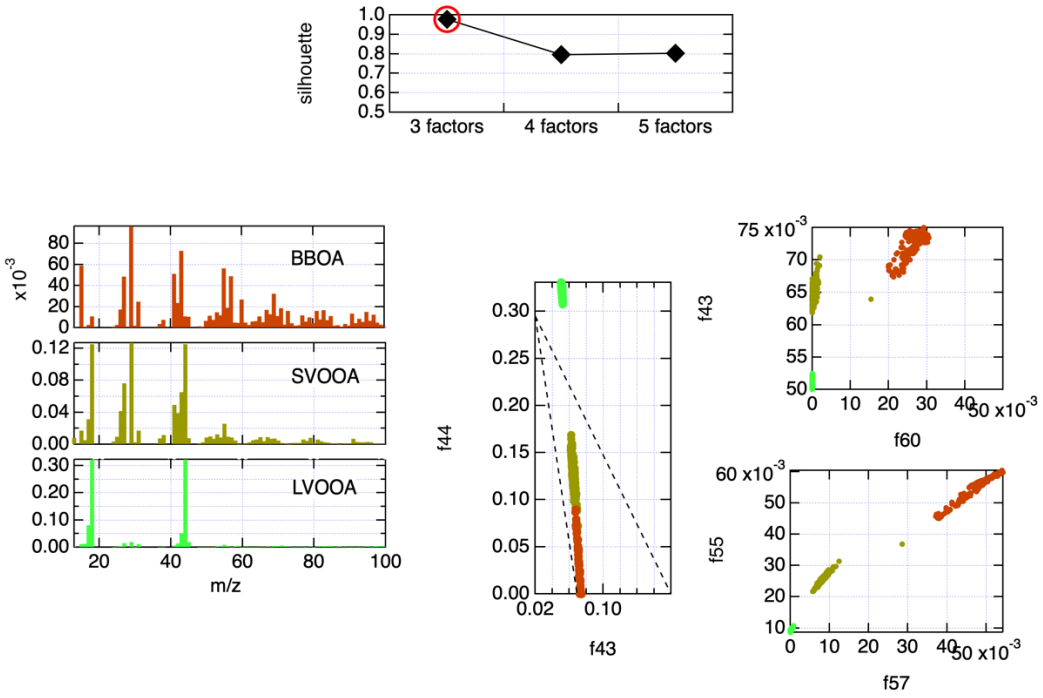

Supplemental Figure S5. K-means clustering results for March-May (spring) period.

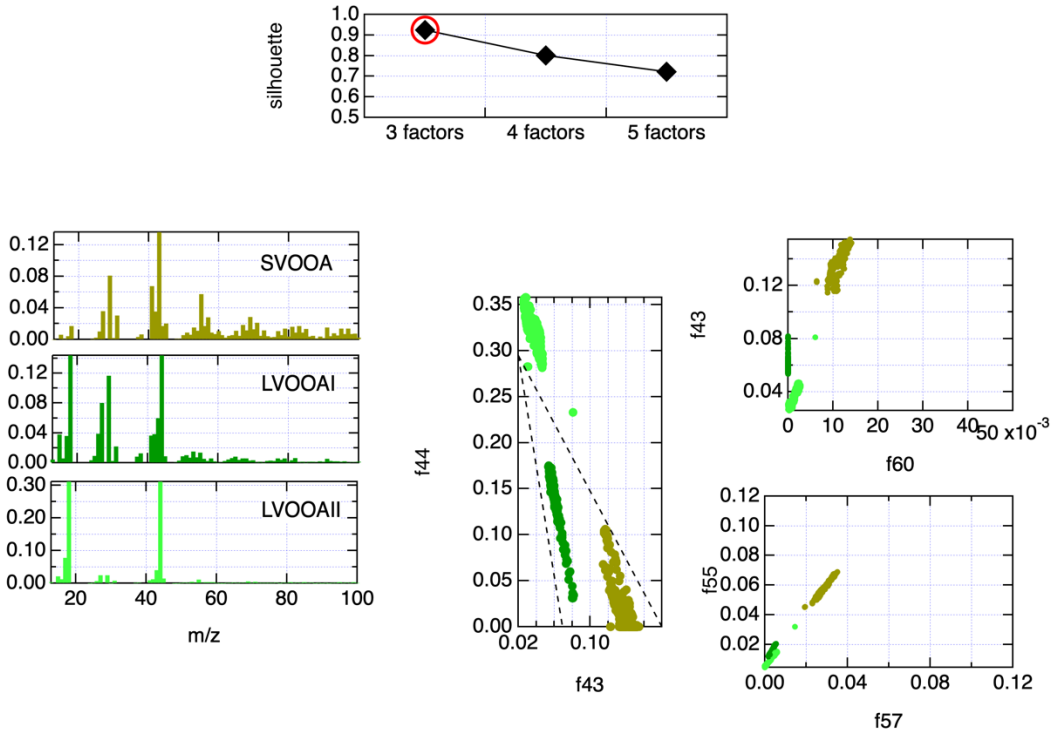

115 **Supplemental Figure S6.** K-means clustering results for June-August (summer) period.

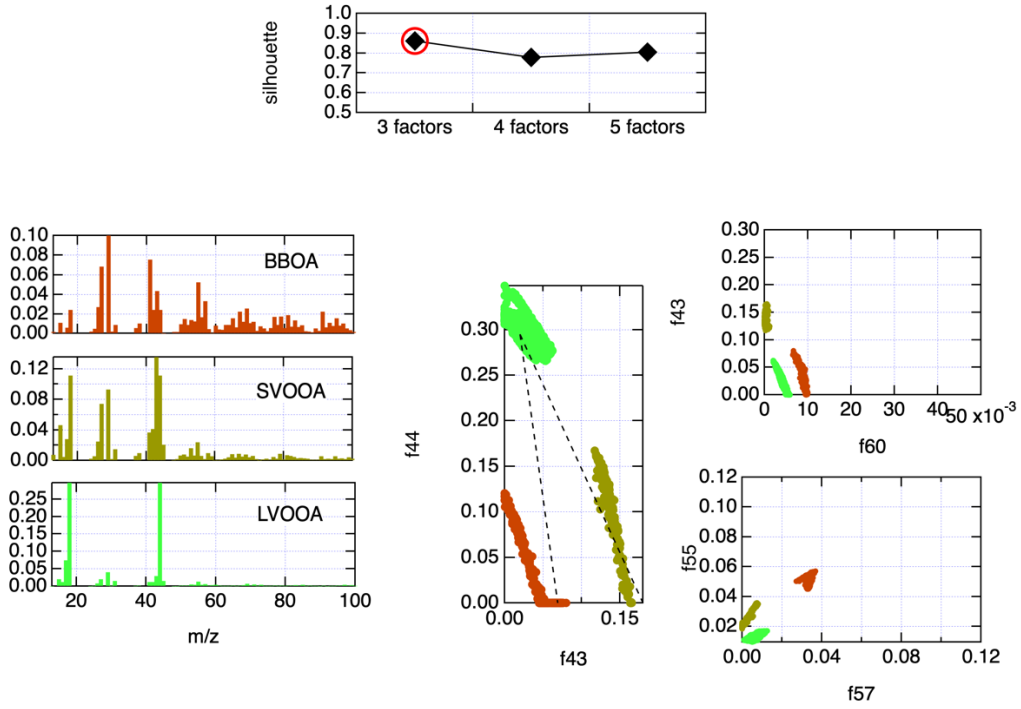

Supplemental Figure S7. K-means clustering results for September-November (autumn) period.

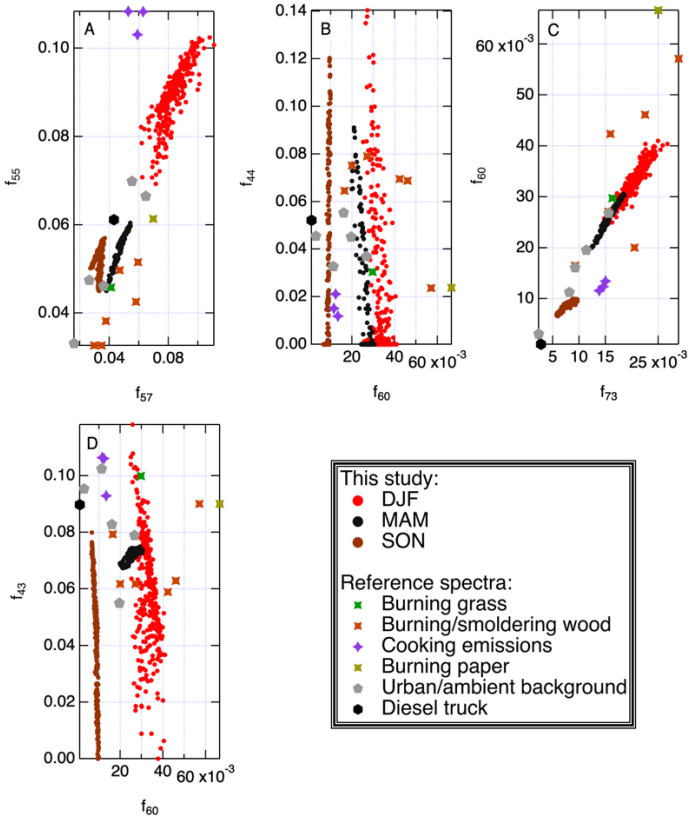

Supplemental Figure S8. Plots of characteristic markers for BBOA for the BBOA PMF factors obtained from seasonal analysis of the SGP dataset.

Each of the seasonal sets of reference profiles includes a profile identified as semi-volatile oxidized organic aerosol (SVOOA), and at least one profile identified as low-volatility oxidized organic aerosol (LVOOA). Winter, spring and autumn reference profiles also include a factor identified as biomass burning organic aerosol (BBOA). The identities of these profiles have been established based on comparisons with AMS/ACSM literature. In particular, we use a database of published AMS/ACSM reference mass spectra described in Jeon et al. (2023) to carry out a comparison of our BBOA and SVOOA reference profiles to previous field and laboratory studies as shown in Supplemental Tables S2 and S3 and Supplemental Figure S9. We use a average BBOA and SVOOA profiles across all SGP seasons shown in Supplemental Figure S10 to carry out the comparisons.

Supplemental Table S2. AMS database spectra most closely matching the SGP SVOOA reference profile.

Reference description	Lab/ambient	Reference citation	Cosine similarity score
α-terpinene oxidized with O3	Lab	Bahreini et al. (2005)	0.9857
Terpinolene oxidized with O3	Lab	Bahreini et al. (2005)	0.9789
α-pinene oxidized with O3	Lab	Bahreini et al. (2005)	0.9769
β-caryophyllene oxidized with O3	Lab	Bahreini et al. (2005)	0.9683
Average SVOOA factor from multiple ambient datasets (global)	Ambient	Ng et al. (2011)	0.9672
Diesel exhaust	Lab	Sage et al. (2007)	0.9648
Myrcene oxidized with O3	Lab	Bahreini et al. (2005)	0.9627
Methylcyclohexene oxidized with O3	Lab	Bahreini et al. (2005)	0.9567
β-pinene oxidized with O3	Lab	Bahreini et al. (2005)	0.9528
Median SVOOA from EUCARRI 2008-2009 campaigns (continental Europe)	Ambient	Crippa et al. (2014)	0.9512

Supplemental Table S3. AMS database spectra most closely matching the SGP BBOA reference profile.

Reference description	Lab/ambient	Reference citation	Cosine similarity score
Cooking Organic Aerosol (COA) factor, Paris, winter, 2010	Ambient	Crippa et al., 2013	0.9465
Chicken cooked on propane grill (no skin)	Lab	Mohr et al., 2009	0.9432
Cooking Organic Aerosol (COA) factor, Rome (urban), summer, 2014	Ambient	Struckmeier et al., 2016	0.9427
Octadecanoic (Stearic) acid	Lab	Alfarra, 2004	0.9419
Myristic acid	Lab	Alfarra, 2004	0.9409
Average BBOA factor from multiple ambient datasets (global)	Ambient	Ng et al. (2011)	0.9371
Cooking Organic Aerosol (COA) factor, Rome (suburban), summer, 2014	Ambient	Struckmeier et al., 2016	0.9350
Biomass burning: Savanna Grass	Lab	Schneider et al., 2006	0.9331
Urban background, Vancouver	Ambient	Alfarra, et al., 2004	0.9313
Diesel Exhaust	Lab	Sage et al. (2007)	0.9298

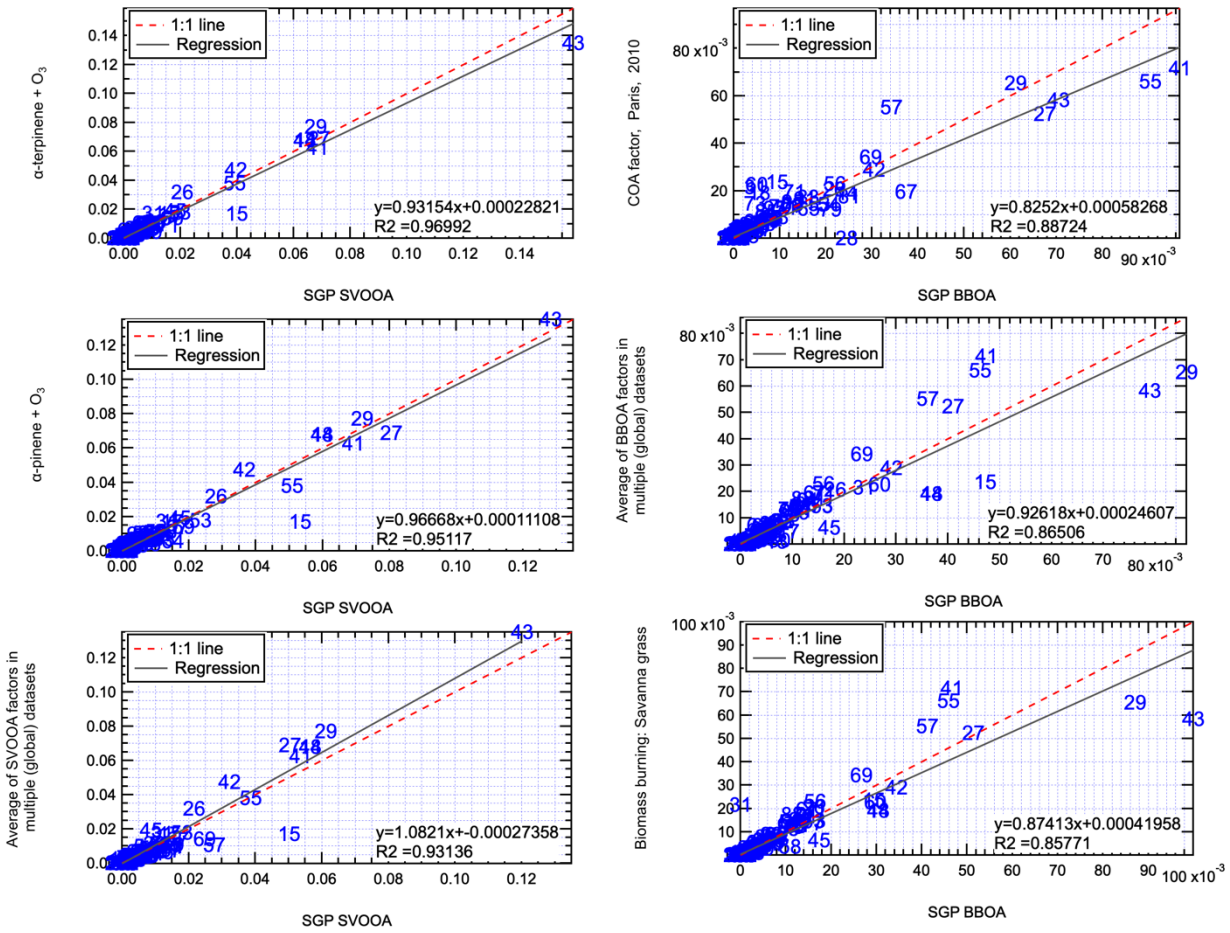

Supplemental Figure S9. Regression plots for selected AMS database spectra and SGP SVOOA and BBOA reference profiles.

The SGP reference profile identified as SVOOA matches well with ambient SVOOA averaged from both global (Ng et al., 2011) and European (Crippa et al., 2014) datasets, but also multiple laboratory examples of oxidized monoterpene SOA (Bahreini et al., 2005). The SGP reference profile identified as BBOA shows a strong m/z 60 levoglucosan marker signal (Supplemental Figures S4 – S7 and S8) associated with BBOA and a strong correlation with ambient BBOA factor averaged from a global dataset (Ng et al., 2011). The SGP BBOA profile also strongly correlates with both laboratory and field examples of cooking organic aerosol (COA) (Crippa et al., 2013; Mohr et al., 2009; Struckmeier et al., 2016), which is not necessarily as expected as the SGP BBOA is more likely to be produced by agricultural burning.

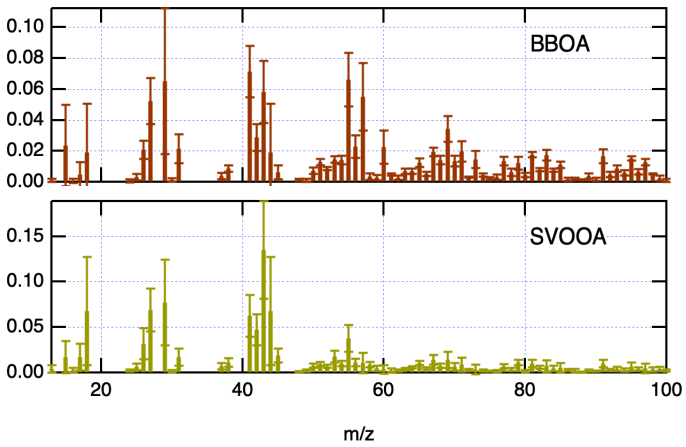

Supplemental Figure S10. Reference profiles used for the constrained ME-2 PMF analysis. Error bars are 1σ standard deviations.

S2.2 Constrained Rolling PMF

Rolling PMF is carried out on the ACSM organic matrix and its corresponding error matrix at the native sampling resolution of 30 minutes. The m/z 16, 17, 18 and 28, which are replicates of the variability in m/z 44 were removed from the PMF calculation and recalculated a posteriori as a function of the m/z 44 contribution attributed to each factor profile (Elser et al., 2016). The m/z 12 has been removed from the PMF calculation permanently, as it often becomes negative. A down weighing function of the form of 1/S2N was applied for signal-to-noise (S2N) ratios lower than 1 and untouched otherwise (Visser et al., 2015) on each cell of the organic matrix separately. A rolling window of 5 days with a 1-day shift was used for the rolling strategy. Each rolling window run was initialized 10 times. The total number of individual PMF runs performed was 8810. From the seasonal pre-tests shown in Supplemental Figures S4-S7, it is evident that each season contains LVOOA and SVOOA factors, but only winter, spring and autumn contain BBOA. In order to avoid over-fitting the BBOA factor for seasons where no such factor is present, we test two different rolling solutions: (1) a 2 factor solution with constrained SVOOA factor (shown in Supplemental Figure S10) and an unconstrained LVOOA factor and (2) a 3 factor solution with constrained SVOOA and BBOA factors (shown in Supplemental Figure S10) and an unconstrained LVOOA factor. For the constrained factors, we use the a-value approach (Crippa et al., 2014) to allow variability in the constraints. Following Canonaco et al. (2021), we use a random a-value between 0.1 and 0.6 (with a step 0.01) for each rolling window.

The final rolling solution was computed as follows. For each rolling window of the 3 factor solution with BBOA, we calculated the explained variation in m/z 60 by the BBOA factor:

$$EV_{j,k} = \frac{\sum_{i=1}^{n}(|g_{ik} \cdot f_{kj}|/\sigma_{ij})}{\sum_{i=1}^{n}\left((\sum_{h=1}^{p}|g_{ih} \cdot f_{hj}| + e_{ij})/\sigma_{ij}\right)}.$$

The distribution of explained variation values for m/z 60 is shown in Supplemental Figure S11.

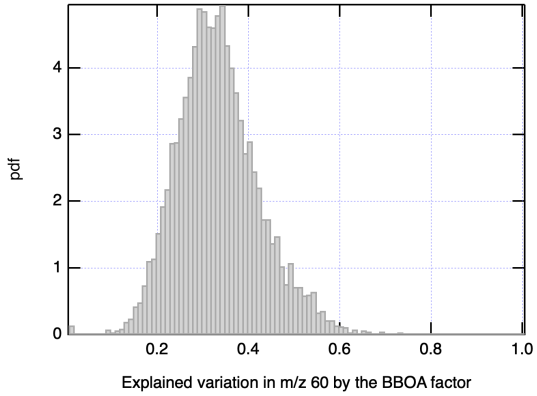

Supplemental Figure S11. Distribution of explained variation in m/z 60 by the BBOA factor in the 3 factor solution.

Here we consider BBOA to be present if at least 30% of the variability in m/z 60 is explained by the BBOA factor. For those windows, we use the 3 factor solution. In all other cases, we use the 2 factor solution and set the time series contribution of BBOA to 0. Supplemental Figure S12 shows the distribution of some of the key markers in factors fitted in each window selected for further processing.

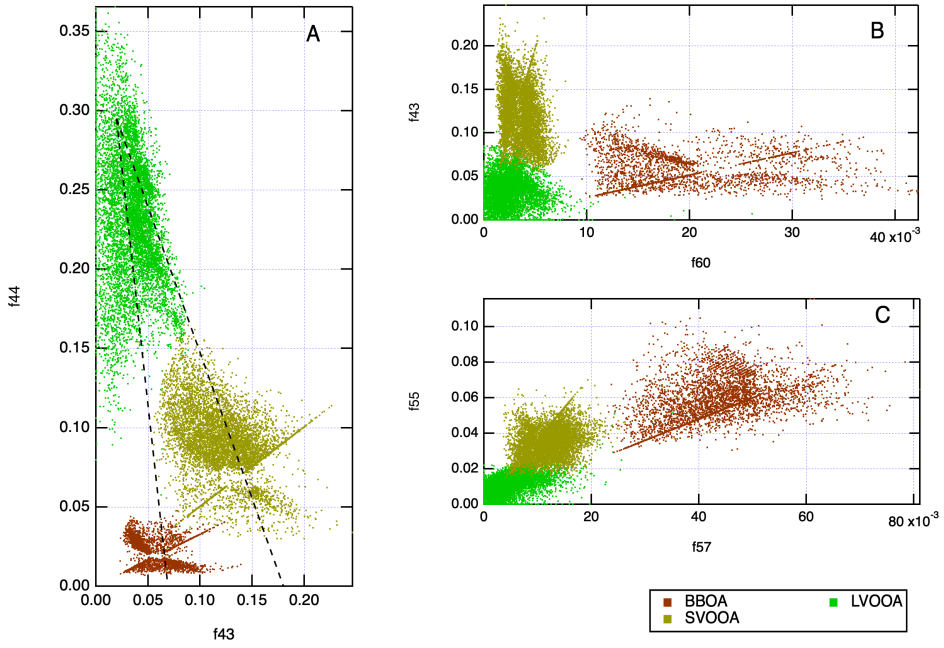

Supplemental Figure S12. Distributions of f43, f44, f55, f57 and f60 in all PMF solutions.

The final step before averaging the solution is rejection of outlier solution windows performed using one-class support vector machines (SVM), a type of unsupervised outlier detection algorithm (Hejazi and Singh, 2013). In this case, the one-class SVM is performed with a radial basis function kernel on each of the constrained and unconstrained factors separately using a reduced feature space containing only f43, f44, f55, f57 and f60. Supplemental Figure S13 shows which points were marked as outliers and rejected from the final PMF solution.

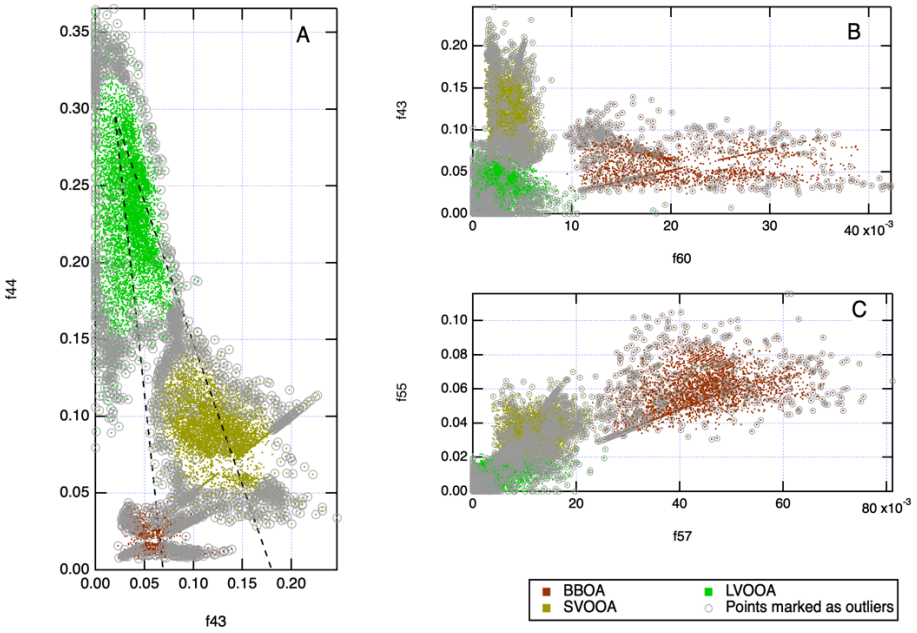

Supplemental Figure S13. As in Supplemental Figure 8, but the outliers detected by the one-class SVM algorithm are circled in gray.

In rolling PMF, each time point is associated with ~50 PMF solutions, which are averaged to arrive at the final answer. We also compute the standard deviations at each time point to estimate the relative PMF error, as defined in Canonaco et al. (2021) as shown in Supplemental Figure S14. The centers of the log-normal fits are ±57%, ±35% and ±13% for BBOA, SVOOA and LVOOA, respectively.

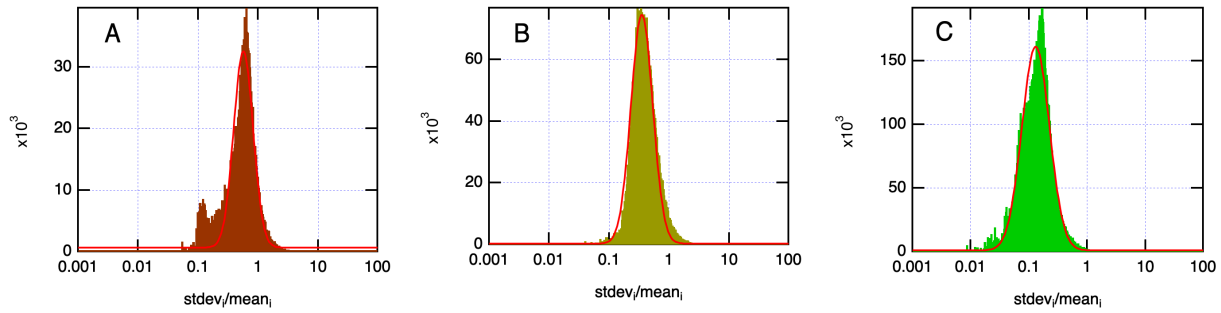

Supplemental Figure S14. Estimate of relative PMF error of each averaged solution, as defined by Canonaco, et al. (2021). The fits shown are lognormal.

The averaged time series and factor profiles can be used together with the organic matrix and its uncertainty matrix to calculate the residual matrix **E** (equation 1) and scaled residuals (e_{ij}/σ_{ij}). Those are plotted as total histograms and statistics over the m/z's and time in Supplemental Figure S15.

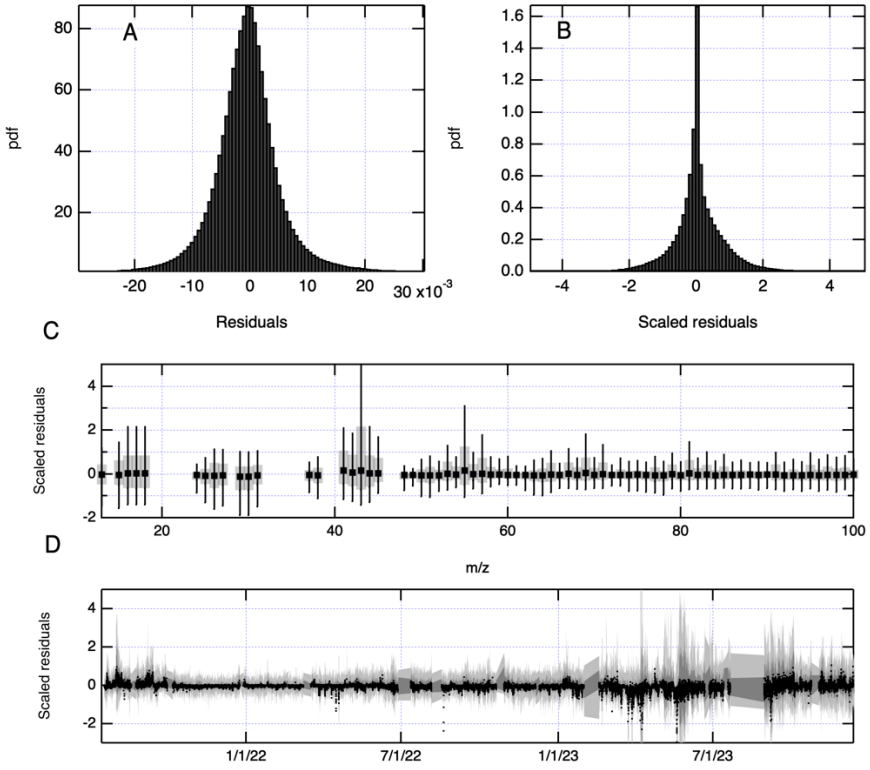

Supplemental Figure S15. Residual analysis of the averaged PMF solution.

The scaled residuals are distributed around 0, not revealing any systematic over- or under-estimation. The distribution of the scaled residuals almost always falls between ±2, with ±3 being a reasonable range for scaled residuals as defined in Paatero and Hopke (2009). The highest residuals generally occur during transient periods of high aerosol loadings, such as biomass burning events, which are influenced by short-time sources, which are difficult to capture in a PMF analysis.

S3 N_{CCN}/N_{CN} vs. supersaturation during smoky and non-smoky periods

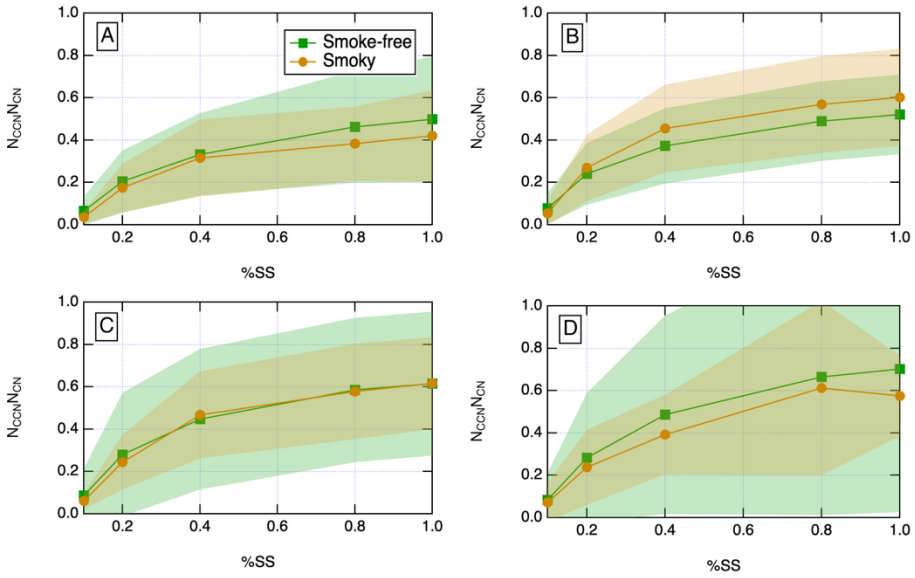

Supplemental Figure S16. A comparison of N_{CCN}/N_{CN} at different supersaturations during smoky and smoke-free periods at SGP. A: DJF, B: MAM, C: JJA, D: SON.

S4 Temporal distribution of fire events

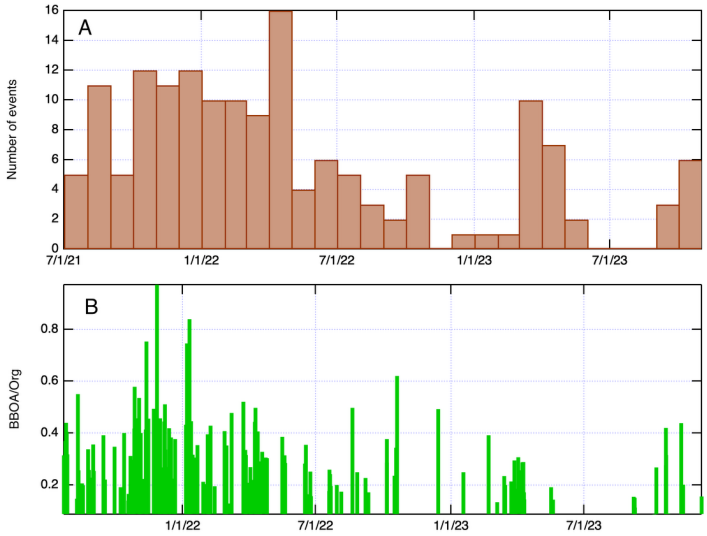

Supplemental Figure S17. A. Number of fire events detected each month. B. BBOA/Org ratios of peak of each BBOA event

S5 Classification of local vs. regional synoptic conditions

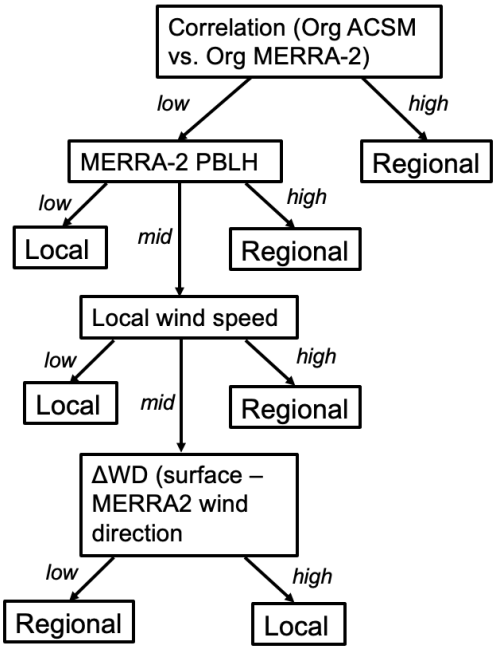

Supplemental Figure S18. Decision tree used to classify fire events into local vs. regional

We classified each observation as belonging to either a local or a regional regime using a fixed-order decision-tree classifier (Supplemental Figure S18) applied to the synchronized time series. The classifier used four predictors: (1) the rolling correlation between in situ ACSM organic and MERRA-derived OC, (2) MERRA-2 planetary boundary layer height (PBLH), (3) wind speed, and (4) the absolute wind-direction difference between the in situ and MERRA wind fields (ΔWD). Wind speed was taken from the in-situ record when available, with the MERRA value used only to fill missing data. The ACSM organic – MERRA-2 OC correlation term was computed using a centered 24 hour rolling window, and ΔWD was calculated as the circular angular difference on a 0–180° scale.

Rather than using fixed, pre-defined cutoff values, the decision boundaries were estimated from the data itself. Specifically, lower and upper thresholds for the rolling Org–MERRA correlation, PBLH, wind speed, and ΔWD were computed from the empirical distribution of each variable.

The decision tree was then evaluated sequentially, with the first decisive branch determining the regime assignment (Supplemental Figure S18). High Org–MERRA correlation was interpreted as evidence of regional behavior, whereas low correlation indicated local influence. If the correlation was intermediate or missing, the algorithm next evaluated PBLH, with relatively deeper boundary layers favoring the regional class and shallower boundary layers favoring the local class. If PBLH was also inconclusive, wind speed was considered, with stronger winds indicating regional conditions and weaker winds indicating local conditions. Finally, if the first three predictors remained ambiguous, the classifier used wind-direction agreement: small directional differences between in situ and MERRA winds were classified as regional, whereas large differences were classified as local. If none of the four predictors produced a decisive outcome, the final label was assigned from the midpoint of the correlation thresholds; if correlation was unavailable, the observation defaulted to the regional class.

References

Bahreini, R., Keywood, M. D., Ng, N. L., Varutbangkul, V., Gao, S., Flagan, R. C., Seinfeld, J. H., Worsnop, D. R., and Jimenez, J. L.: Measurements of Secondary Organic Aerosol from Oxidation of Cycloalkenes, Terpenes, and *m* -Xylene Using an Aerodyne Aerosol Mass Spectrometer, Environ. Sci. Technol., 39, 5674–5688, https://doi.org/10.1021/es048061a, 2005.

Canonaco, F., Crippa, M., Slowik, J. G., Baltensperger, U., and Prévôt, A. S. H.: SoFi, an IGOR-based interface for the efficient use of the generalized multilinear engine (ME-2) for the source apportionment: ME-2 application to aerosol mass spectrometer data, Atmos. Meas. Tech., 6, 3649–3661, https://doi.org/10.5194/amt-6-3649-2013, 2013.

Canonaco, F., Tobler, A., Chen, G., Sosedova, Y., Slowik, J. G., Bozzetti, C., Daellenbach, K. R., El Haddad, I., Crippa, M., Huang, R.-J., Furger, M., Baltensperger, U., and Prévôt, A. S. H.: A new method for long-term source apportionment with time-dependent factor profiles and uncertainty assessment using SoFi Pro: application to 1 year of organic aerosol data, Atmos. Meas. Tech., 14, 923–943, https://doi.org/10.5194/amt-14-923-2021, 2021.

Crippa, M., DeCarlo, P. F., Slowik, J. G., Mohr, C., Heringa, M. F., Chirico, R., Poulain, L., Freutel, F., Sciare, J., Cozic, J., Di Marco, C. F., Elsasser, M., Nicolas, J. B., Marchand, N., Abidi, E., Wiedensohler, A., Drewnick, F., Schneider, J., Borrmann, S., Nemitz, E., Zimmermann, R., Jaffrezo, J.-L., Prévôt, A. S. H., and Baltensperger, U.: Wintertime aerosol chemical composition and source apportionment of the organic fraction in the metropolitan area of Paris, Atmos. Chem. Phys., 13, 961–981, https://doi.org/10.5194/acp-13-961-2013, 2013.

Crippa, M., Canonaco, F., Lanz, V. A., Äijälä, M., Allan, J. D., Carbone, S., Capes, G., Ceburnis, D., Dall'Osto, M., Day, D. A., DeCarlo, P. F., Ehn, M., Eriksson, A., Freney, E., Hildebrandt Ruiz, L., Hillamo, R., Jimenez, J. L., Junninen, H., Kiendler-Scharr, A., Kortelainen, A.-M., Kulmala, M., Laaksonen, A., Mensah, A. A., Mohr, C., Nemitz, E., O'Dowd, C., Ovadnevaite, J., Pandis, S. N., Petäjä, T., Poulain, L., Saarikoski, S., Sellegri, K., Swietlicki, E., Tiitta, P., Worsnop, D. R., Baltensperger, U., and Prévôt, A. S. H.: Organic aerosol components derived from 25 AMS data sets across Europe using a consistent ME-2 based source apportionment approach, Atmos. Chem. Phys., 14, 6159–6176, https://doi.org/10.5194/acp-14-6159-2014, 2014.

Elser, M., Bozzetti, C., El-Haddad, I., Maasikmets, M., Teinemaa, E., Richter, R., Wolf, R., Slowik, J. G., Baltensperger, U., and Prévôt, A. S. H.: Urban increments of gaseous and aerosol pollutants and their sources using mobile aerosol mass spectrometry measurements, Atmos. Chem. Phys., 16, 7117–7134, https://doi.org/10.5194/acp-16-7117-2016, 2016.

Hejazi, M. and Singh, Y. P.: ONE-CLASS SUPPORT VECTOR MACHINES APPROACH TO ANOMALY DETECTION, Applied Artificial Intelligence, 27, 351–366, https://doi.org/10.1080/08839514.2013.785791, 2013.

Jeon, S., Walker, M. J., Sueper, D. T., Day, D. A., Handschy, A. V., Jimenez, J. L., and Williams, B. J.: A searchable database and mass spectral comparison tool for the Aerosol Mass Spectrometer (AMS) and the Aerosol Chemical Speciation Monitor (ACSM), Atmos. Meas. Tech., 16, 6075–6095, https://doi.org/10.5194/amt-16-6075-2023, 2023.

Kulkarni, G., Mei, F., Shilling, J. E., Wang, J., Reveggino, R. P., Flynn, C., Zelenyuk, A., and Fast, J.: Cloud Condensation Nuclei Closure Study Using Airborne Measurements Over the Southern Great Plains, JGR Atmospheres, 128, e2022JD037964, https://doi.org/10.1029/2022JD037964, 2023.

Middlebrook, A. M., Bahreini, R., Jimenez, J. L., and Canagaratna, M. R.: Evaluation of Composition-Dependent Collection Efficiencies for the Aerodyne Aerosol Mass Spectrometer using Field Data, Aerosol Science and Technology, 46, 258–271, https://doi.org/10.1080/02786826.2011.620041, 2012.

Mohr, C., Huffman, J. A., Cubison, M. J., Aiken, A. C., Docherty, K. S., Kimmel, J. R., Ulbrich, I. M., Hannigan, M., and Jimenez, J. L.: Characterization of Primary Organic Aerosol Emissions from Meat Cooking, Trash Burning, and Motor

Vehicles with High-Resolution Aerosol Mass Spectrometry and Comparison with Ambient and Chamber Observations, Environ. Sci. Technol., 43, 2443–2449, https://doi.org/10.1021/es8011518, 2009.

Ng, N. L., Canagaratna, M. R., Jimenez, J. L., Zhang, Q., Ulbrich, I. M., and Worsnop, D. R.: Real-Time Methods for Estimating Organic Component Mass Concentrations from Aerosol Mass Spectrometer Data, Environ. Sci. Technol., 45, 910–916, https://doi.org/10.1021/es102951k, 2011.

Paatero, P.: The Multilinear Engine—A Table-Driven, Least Squares Program for Solving Multilinear Problems, Including the *n* -Way Parallel Factor Analysis Model, Journal of Computational and Graphical Statistics, 8, 854–888, https://doi.org/10.1080/10618600.1999.10474853, 1999.

Paatero, P. and Hopke, P. K.: Rotational tools for factor analytic models, Journal of Chemometrics, 23, 91–100, https://doi.org/10.1002/cem.1197, 2009.

Paatero, P. and Tapper, U.: Positive matrix factorization: A non-negative factor model with optimal utilization of error estimates of data values, Environmetrics, 5, 111–126, https://doi.org/10.1002/env.3170050203, 1994.

Petters, M. D. and Kreidenweis, S. M.: A single parameter representation of hygroscopic growth and cloud condensation nucleus activity, Atmos. Chem. Phys., 7, 1961–1971, https://doi.org/10.5194/acp-7-1961-2007, 2007.

Struckmeier, C., Drewnick, F., Fachinger, F., Gobbi, G. P., and Borrmann, S.: Atmospheric aerosols in Rome, Italy: sources, dynamics and spatial variations during two seasons, Atmos. Chem. Phys., 16, 15277–15299, https://doi.org/10.5194/acp-16-15277-2016, 2016.

Ulbrich, I. M., Canagaratna, M. R., Zhang, Q., Worsnop, D. R., and Jimenez, J. L.: Interpretation of organic components from Positive Matrix Factorization of aerosol mass spectrometric data, Atmos. Chem. Phys., 9, 2891–2918, https://doi.org/10.5194/acp-9-2891-2009, 2009.

Visser, S., Slowik, J. G., Furger, M., Zotter, P., Bukowiecki, N., Canonaco, F., Flechsig, U., Appel, K., Green, D. C., Tremper, A. H., Young, D. E., Williams, P. I., Allan, J. D., Coe, H., Williams, L. R., Mohr, C., Xu, L., Ng, N. L., Nemitz, E., Barlow, J. F., Halios, C. H., Fleming, Z. L., Baltensperger, U., and Prévôt, A. S. H.: Advanced source apportionment of size-resolved trace elements at multiple sites in London during winter, Atmos. Chem. Phys., 15, 11291–11309, https://doi.org/10.5194/acp-15-11291-2015, 2015.

Vu, D., Gao, S., Berte, T., Kacarab, M., Yao, Q., Vafai, K., and Asa-Awuku, A.: External and internal cloud condensation nuclei (CCN) mixtures: controlled laboratory studies of varying mixing states, Atmos. Meas. Tech., 12, 4277–4289, https://doi.org/10.5194/amt-12-4277-2019, 2019.

Zhang, Q., Jimenez, J. L., Canagaratna, M. R., Ulbrich, I. M., Ng, N. L., Worsnop, D. R., and Sun, Y.: Understanding atmospheric organic aerosols via factor analysis of aerosol mass spectrometry: a review, Anal Bioanal Chem, 401, 3045–3067, https://doi.org/10.1007/s00216-011-5355-y, 2011.